

# Chapter 11

## ETEM Studies of Electrodes and Electro-catalysts

Christian Jooss, Stephanie Mildner, Marco Beleggia, Daniel Mierwaldt, and Vladimir Roddatis

**Abstract** Environmental TEM is an excellent tool for gaining insight into the atomic and electronic structure of electro-catalysts under operating conditions. Several electrochemical reactions such as oxidation/reduction processes of electrodes, heterogeneous gas phase catalysis of water splitting/oxygen evolution and electrochemical corrosion processes of materials have been studied in some pioneering experiments which will be summarized in this chapter. These experiments often reveal a strong change of the electrode due to the adsorption of gas species from the environment as well as due to the impact of the electron beam. We show that inelastic scattering of the high-energy electrons can induce electric potentials in the studied samples influencing the observed state of the catalyst. After an introduction to electrochemistry and ETEM investigations, we address, experimentally and theoretically, beam-induced potentials, their dependence on several parameters such as electron flux, electric conductivity, and geometry of samples, aiming at learning how to disentangle them from radiation damage. Our second focus is to control the electric potential distribution within and around samples by dedicated electrical TEM sample holders. To illustrate how this can be achieved, we present the results of a bias-controlled electro-corrosion experiment. We will discuss some of the main experimental and theoretical challenges for the development of controlled electrochemistry studies in transmission electron microscopes.

---

C. Jooss (✉) • S. Mildner • D. Mierwaldt • V. Roddatis  
Institute of Materials Physics, University of Goettingen, Friedrich-Hund-Platz 1,  
Goettingen 37077, Germany  
e-mail: [jooss@ump.gwdg.de](mailto:jooss@ump.gwdg.de)

M. Beleggia  
Center for Electron Nanoscopy, Technical University of Denmark, Fysikvej 307,  
Kongens Lyngby 2800, Denmark

Helmholtz-Zentrum Berlin für Materialien und Energie, Hahn-Meitner-Platz 1,  
Berlin 14109, Germany

## 11.1 Introduction into Electro-catalysis

Electrochemistry, i.e., chemical reactions involving electron transfer, has been a subject of scientific investigation for more than 200 years. Its relevance has increased in recent years due to the need of developing a sustainable energy basis. Electrochemical reactions are of tremendous importance in energy storage (e.g., electrolysis, fuel cells, and batteries), controlled low energy conversion of materials (e.g., metal extraction from ores) and are also involved in undesired reactions such as degradation and corrosion. Electro-catalysis is the increase in the rate of an electrochemical reaction induced by the change of reaction barriers due to the involvement of the electrode surface. Real electrode materials, therefore, do not only mediate the electrochemical electron transfer but in many cases also participate as electro-catalysts. The development of suitable electro-catalysts is essential for high efficiency of electrochemical reactions since they allow for controlling the activation barriers for the electron transfer mediated reactions and thus the activity and selectivity of a reaction. Since electro-catalysts are involved in the reaction process, their atomic and electronic structure typically changes substantially in their active state. Consequently, gaining a deeper understanding of catalysts performance in operation requires atomic scale studies under controlled operating conditions, i.e., at defined electrical conditions, redox state, and chemical environments.

### 11.1.1 The Equilibrium State of the Electrode Surface

TEM studies of the near surface atomic and electronic structure of electrodes and electro-catalysts in gas or liquid environments can give rise to fundamentally different results compared to high vacuum environments due to changes in the electrochemical equilibrium state of the electrode. The electrochemical equilibrium at the interface between the electrode and the gas/liquid environment is determined by the adsorption/desorption of environmental gas or liquid species  $g$  at electrode sites  $s$ .



where  $g_a$  denotes the gas atom adsorbed at the surface site  $s_a$ . Both the surface sites and the adsorbed atoms are modified in atomic structure, bonding, and charge state compared to the desorbed configuration. The free enthalpy of adsorption is given by

$$\Delta G = \Delta G_0 + RT \ln \left( \frac{a_g}{a_s} \right) \quad \text{with} \quad \Delta G_0 = \mu_{s_a} - \mu_s + \mu_{g_a} - \mu_g. \quad (11.2)$$

$\mu_i$  denotes the chemical potential of the involved species under standard conditions. In order to find the pressure dependence of  $\Delta G$ , the activities of the gas species and surface sites must be related to the respective surface concentrations  $a_i = \gamma_i c_i$ , via

the activity coefficient  $\gamma_i$ . In the following, we assume that  $\gamma_g = 1$  and that the number of surface sites  $c_s$  does not change with pressure (which may be unrealistic due to adsorption induced changes in surface structure), giving

$$\Delta G = \Delta G_0 + RT \ln \left( \frac{p}{p_0} \right). \quad (11.3)$$

Here,  $p$  denotes the pressure of the gas and  $p_0 = 1$  bar is taken as standard condition. At high enough concentrations of surface adsorbates, gas species can condense into liquid (e.g., for  $\text{H}_2\text{O}$ ) or even solid layers (e.g., for some  $\text{C}_n\text{H}_m$ ).

Generally, the formation of electrochemical equilibrium at the electrode surface is performed by charge transfer between the electrode and the adsorbents forming a space charge layer with a potential drop given by the Nernst equation

$$\Delta\varphi = \frac{\Delta G_0}{nF} + \frac{RT}{nF} \ln \left( \frac{p}{p_0} \right). \quad (11.4)$$

$F$  denotes the Faraday constant and  $n$  the number of moles. The total electric potential drop  $\Delta\varphi = \Delta\phi_s + \Delta\phi_g$  is composed of the potential of the electrode and the adsorbed gas species, respectively, forming a Helmholtz double layer. The electric potential formed in electrochemical equilibrium is controlled by the concentration of surface adsorbents as well as the difference of the electrode's work function and the redox potential of the surface species. Figure 11.1 shows a sketch of such a situation for the example of a perovskite oxide electrode.

We want to emphasize here that this equilibrium state of the electrode in contact with a gaseous or liquid environment is a dynamic state, where the reaction rate of the forward reaction  $k_+ c_s c_g$  and of the backward reaction  $k_- c_{s_a} c_{g_a}$  are equal. Under standard conditions they are related to the equilibrium rate constant by

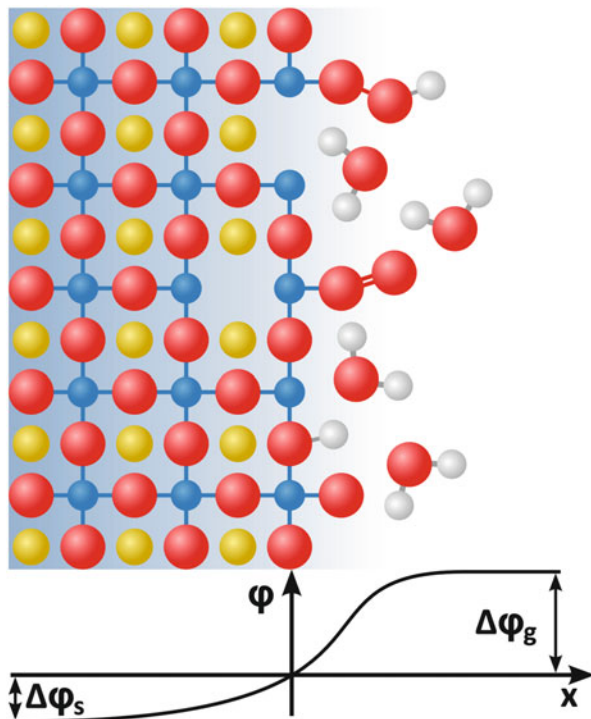
$$k_0 = \frac{k_+}{k_-} = \frac{c_{s_a} c_{g_a}}{c_s c_g} = e^{-\frac{\Delta G_0}{RT}}. \quad (11.5)$$

Consequently, pressure-dependence ETEM observations of electrodes or electro-catalysts even near equilibrium conditions exhibit atomic and electronic double space charge layer like structures which are formed by a dynamical process of gas absorption/desorption with possible surface condensation and induced surface and subsurface reorganization.

### 11.1.2 *Electrochemical Activity Driven by Beam Induced or Applied Electric Potentials*

Electrochemical equilibrium of the electrode in contact with gas/liquid environments in an ETEM can be shifted by the electronic excitations and atomic displacements which are induced by the high-energy electron beam. Emission of excited

**Fig. 11.1** Sketch of the equilibrium state of an electrode surface in contact with water vapor. This example shows a perovskite forming oxygen vacancies and oxygen-based adsorbates leading to a potential drop across the surface



electrons may induce an electric potential at the illuminated sample area. In addition, using appropriate sample holders, an external electric potential can be applied to the TEM sample.

Applying such potentials can give rise to a net charge flow from the electrode to the surface adsorbent and thus to driving a surface redox process. The rate constants for the forward and backward reactions are modified by the application of a potential  $V$  as follows:

$$k_+ = k_+^0 \exp\left[\frac{\alpha F}{RT}(V - V_0)\right] \quad \text{and} \quad k_- = k_-^0 \exp\left[-\frac{(1 - \alpha)F}{RT}(V - V_0)\right] \quad (11.6)$$

leading to a net current density

$$j = \frac{nF}{A} \{k_+ c_s c_g - k_- c_{s_a} c_{g_a}\} \\ = j_0 \left\{ \exp\left[\frac{\alpha F}{RT}(V - V_0)\right] - \exp\left[-\frac{(1 - \alpha)F}{RT}(V - V_0)\right] \right\}, \quad (11.7)$$

known as the Butler–Volmer equation. It describes electrode kinetics for charge transfer limited reactions. The surface area of the electrode is denoted by  $A$ . In the

case of a one electron reaction,  $\alpha$  is called symmetry factor and describes the sensitivity of the transition state to the applied voltage for the forward and backward reactions, respectively. If the effect on the potential barrier is the same for the forward and backward reactions, then  $\alpha = 1 - \alpha = 0.5$ . The exchange current density is related to the equilibrium rate constant by

$$j_0 = \frac{nF}{A} k_0 (c_s c_g)^{1-\alpha} (c_{s_a} c_{g_a})^\alpha \approx \frac{nF}{A} c_s k_0 c_g^{1-\alpha} c_{g_a}^\alpha. \quad (11.8)$$

Note that  $c_s^{1-\alpha} c_{s_a}^\alpha = c_s$  for  $c_s \approx c_{s_a}$ . If the reaction takes place via an activation barrier  $\Delta E_a$ , the equilibrium rate constant is modified to

$$k_0 = k_{00} e^{-\frac{\Delta E_a}{RT}}. \quad (11.9)$$

With  $k_{00}$  denoting an attempt frequency. Electrodes which exhibit pronounced electro-catalytic activity show a reduced activation barrier compared to non-catalytic electrodes.

## 11.2 Critical Assessment of What Kind of Electrochemical Electrode Properties Can Be Observed in ETEM Experiments

Environmental Transmission Electron Microscopy (ETEM) using aberration corrected microscopes offers the opportunity to access the atomic and electronic structure of electro-catalysts as a function of gas species and pressure ranging from high vacuum ( $p \approx 10^{-7}$  mbar) to pressures of about 10 mbar in differentially pumped configurations (Chang et al. 2010; Hansen et al. 2002; Helveg et al. 2004). Using gas or liquid cell holders, the pressure range can be extended to pressures above 1 bar (Creemer et al. 2010). The high spatial resolution capabilities can be combined with a variety of analytical methods for chemical and band structure analysis by using local X-ray and electron energy loss spectroscopy (EELS) (Hansen et al. 2010).

### 11.2.1 Pressure-Dependent Equilibrium State of the Electrode

Observing the atomic and electronic surface and subsurface structure of the equilibrium state of an electrode as a function of gas species and pressure requires guaranteeing low dose conditions specifically valid for maintaining the electrochemical equilibrium. As a first guess we assume that if the deposited energy due to

inelastic scattering of high energy electrons is much smaller than the potential energy of the double charge layer, electrochemical equilibrium is maintained. Another very critical issue for observing pressure-dependent equilibrium states of electrodes is the initial state of the TEM sample. Its surface and subsurface structure may be modified by preparation processes. Consequently, depending on the preparation conditions, the observed structure under high-vacuum conditions typically may not represent the corresponding equilibrium state but a kinetically frozen metastable state. Changing the Gibbs free energy of adsorption by changing the gas pressure may then allow for the observation of transition processes towards the relevant equilibrium state of the electrode interface to the environment. One example presented in Sect. 11.3.2 of this chapter is the oxidation of an oxygen deficient surface layer on a manganite upon increasing water vapor pressure. Here, however, an electron beam is required to drive this reaction.

### ***11.2.2 Control of Sample Potential $V$***

One of the main challenges for ETEM electrochemistry studies is the control of the sample potential, since according to (11.7), it directly drives electrochemical activity of a TEM sample/electrode. The availability of electrical sample holders on the one side offers great opportunities for the application of electric bias to TEM samples and thus to study their structure in contact with reactants as a function of an applied potential (see Sects. 11.3.4 and 11.3.5). On the other hand, understanding and controlling the effect of the high energy electron beam on the catalyst state poses several obstacles since the effect of beam induced sample charging must be well addressed and separated from other beam induced effects such as beam damage (see Sect. 11.4). Despite electron dose, the electric contact conditions and electric conductivity of the TEM sample or TEM grid may have a tremendous effect on the induced potential. Electric potential experiments such as the electrically controlled corrosion of Ca-manganite presented below represent two-electrode experiments, where the sample potential is measured against the TEM ground. Three-electrode experiments, typically performed in electrochemical cells outside TEM in order to get access to the potential drop between the electrode and the electrolyte, are at present out of reach for gas phase ETEM experiments.

### ***11.2.3 Active Sites and States***

Assuming that well-defined electric potential conditions have been established at a TEM sample by either using beam induced or sample holder controlled bias, access to active sites and active states may become achievable. Not all areas of the electrode surface may exhibit the same activity in electro-catalysis. The surface concentration of the active sites  $c_{s_a}$  (here identified as the concentration of sites with

adsorbed gas molecules) may be significantly smaller than the concentration of non-active surface sites  $c_s$ . The concentration of active sites may even change during activation of the catalyst. Typically, since electro-catalysts are partially involved in the reaction process, their atomic and electronic structure can substantially change during activation (Hutchings et al. 1994; Trotochaud and Boettcher 2014). Even one of the most studied noble metal catalysts, i.e., Pt, shows structural transformation upon polarization, such as the formation of Pt surface oxides even below the threshold of oxygen evolution (Arrigo et al. 2013). In situ XPS shows that CO-oxidation at Pd surfaces requires the formation of a highly reactive PdO surface (Blomberg et al. 2013). In situ X-ray absorption studies reveal that  $\text{Co}_3\text{O}_4$  catalysts can change in Co valence as well as surface coordination in oxidizing or reducing environments (Zheng et al. 2011). In Sect. 11.3.1 of this chapter, an example of an ETEM study of the nucleation of an oxide wetting layer at a surface step of metallic Cu is shown. Understanding the detailed structure and nature of the active site is a central paradigm in modern molecular- or atomic-level catalysis.

### 11.2.4 Turn Over

The turn over frequency  $\text{TOF} = R_{\text{net}}/s_a$  is defined as the number of reactions per active site per time, whereas the turn over number  $\text{TON} = g_a^*/s_a$  of a catalyst can be defined as the number of reacted gas molecules per number of active catalyst sites before it corrodes. A serious limitation for the determination of these numbers in ETEM experiments is the large gas volume compared to very small amounts of catalyst material in TEM samples. A coarse estimate of the number of reacted gas species via an ideal catalyst TEM specimen with  $\text{TOF} = 0.01$  1/s, size of  $1 \mu\text{m} \times 1 \mu\text{m} \times 100 \text{ nm}$  and fraction of active sites  $s_a = 1$  with a density of  $1/(5 \text{ \AA})^2$  shows that one has to accumulate reaction products for  $>5$  min in order to be able measuring concentration changes in the order of 1 % at a total gas pressure of 1  $\mu\text{bar}$ . This does not rule out measuring reaction products in differentially pumped ETEM experiments via the mounted mass spectrometers. However, any quantification of  $\text{TOF}$ 's or  $\text{TON}$ 's via such a configuration is hardly possible. The gas volume can be significantly reduced using gas or liquid cell sample holders (Zandbergen 2012; Kein et al. 2011). However, as we will show by experiments using a sacrificial agent in order to monitor catalytic activity by the growth of a solid phase on top of the electrode, rough estimates of  $\text{TON}$ 's are possible (Sect. 11.3.3).

### 11.2.5 Transient and Transition States

Microscopically, the presence of an activation barrier is due to complex atomic and electronic dynamics, which evolve during the charge transfer and the related oxidation/reduction reaction at the electrode surface. Such transient states can result

in a rich activation barrier landscape. The transition state is defined as the state along the reaction coordinate which has the highest potential energy. It may involve non-equilibrium atomic structure, electronic excitations, and electron-lattice-coupled dynamics at the electrode surface as well as in the reacted species. Simple theories, such as transition state theory (Truhlar et al. 1996), are based on strong assumptions, such as the absence of recrossing of the barrier, the presence of Boltzmann-like equilibrium distribution of energies, and a classical motion over a rigid barrier. Since charge transfer happens on time scales of fs to ns, ETEM is not suitable to directly access such processes. However, observation of transient states during slowly evolving electrochemical oxidation or reduction processes such as observed during oxidation of metal surfaces (Sect. 11.3.1) or during lithiation (Sect. 11.3.5) is already possible. In future, electrochemical studies with ultrafast electron microscopy may build a pathway to directly access ultrafast structure and electronic changes related to charge transfer dynamics.

## 11.3 Case Studies of Model Systems

### 11.3.1 *In Situ Studies of Thermally Activated Redox Reactions*

Electrochemical reactions can be studied in ETEM even in the absence of an externally applied or beam induced electric potentials either by changing the partial pressure of an oxidizing/reducing gas species or by changing the sample temperature. Changing the gas pressure directly modifies the Gibbs free energy (11.3), thus inducing an electrochemical non-equilibrium state that can drive a redox reaction until a new equilibrium is established. If the reaction is kinetically limited, an increase of temperature can dramatically increase the reaction constant (11.9) and thus enabling ETEM observations in a reasonable time scale. In addition, temperature changes may modify the Gibbs free energy of the interface.

Oxidation of metal surfaces requires the transfer of electrons from the metal to the oxygen atoms. Such reactions are often accompanied by complex structure and morphology changes. Zhou et al. (2013) have observed the formation of oxide islands during the oxidation of Cu surfaces via in situ ETEM studies (Fig. 11.2). The growth of islands follows the formation of a  $\text{Cu}_2\text{O}$  wetting layer of thickness of a few atomic layers on the virgin Cu surface. The study shed light onto the preferential formation of the oxide at Cu surface steps and the role of  $\text{Cu}_2\text{O}$ -Cu interfacial strain on the transition from layer to island growth. The experiments were performed at elevated temperatures and an oxygen partial pressures  $p_{\text{O}_2}$  in the range of several  $\mu\text{bar}$ .

The growth of a metal oxide layer due to oxidation of a metal surface requires the migration of either metal cations or oxygen anions through the oxide layer. In situ ETEM oxidation studies of Ni and NiCr alloys were able to shed light onto the



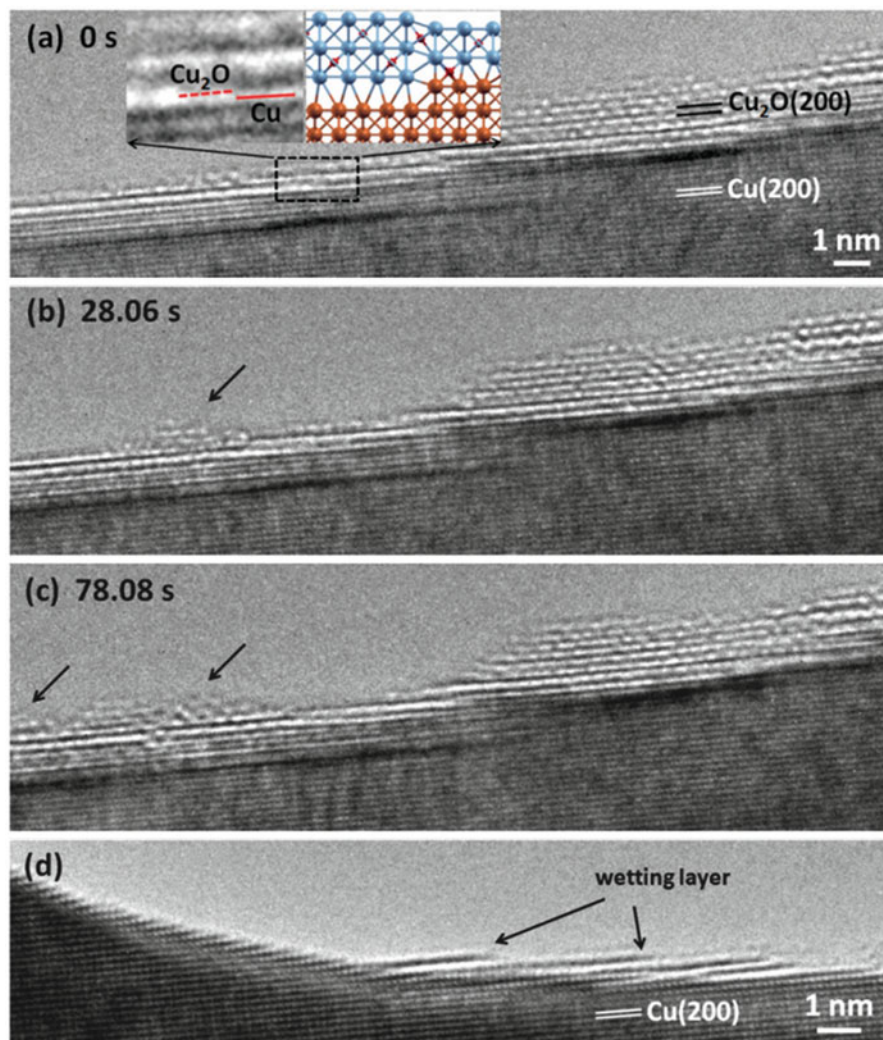


**Fig. 11.2** (a–c) In situ TEM observations of the nucleation and growth of a Cu<sub>2</sub>O island on the oxide wetting layer during oxidation of Cu(100) at 350 °C and  $p_{O_2} = 6.7$  mbar. *Inset in (a)* shows the formation of a disconnection at the buried Cu–Cu<sub>2</sub>O interface due to the presence of an atomic Cu surface step. **(d)** TEM image revealing that the oxide wetting layers initiate at Cu surface steps (Reproduced with permission (pending) from G. Zhou et al. Chem. Commun., 2013, 49, 10862)

role of vacancy injection for the oxidation process (Chenna and Crozier 2012; Wang et al. 2014). The study of SiO<sub>2</sub> supported Ni nanoparticles in a mixture of O<sub>2</sub> and CH<sub>4</sub> in a temperature range between 400 and 500 °C showed that the formation and growth of NiO happens via the migration of Ni atoms through the oxide layer which gives rise to the development of large voids within the oxidized nanoparticles

(Chenna and Crozier 2012). Remarkably, reduction of such NiO shell-void structures in  $\text{CH}_4$  forms metallic Ni at the interior of the particles. The in situ ETEM study of NiCr particle oxidation in 1 mbar of an  $\text{O}_2$  and Ar gas mixture at elevated temperatures reveals preferential oxidation of Cr and void formation due to vacancy injection (Wang et al. 2014). ETEM studies of oxidation and reduction processes thus enable to study a variety of transient states which evolve until completion of the reaction.

### 11.3.2 Manganese Oxide Redox Reactions via Beam Induced Potentials

Oxidation of an oxygen depleted manganite area can be studied by observation of the recrystallization of an initially amorphous edge of a  $\text{Pr}_{1-x}\text{Ca}_x\text{MnO}_3$  (PCMO) film on MgO substrate in contact with pure water vapor as depicted in Fig. 11.3. We have selected an approximately 50 nm thick crystalline sample which is covered by an up to 3 nm thick surface layer of ion beam damaged, amorphous PCMO. The thickness of the layer was measured under high vacuum conditions, where no changes were observed on time scales of 30 min during irradiation with 300 keV electrons. During the exposure to pure water vapor at a pressure of  $p(\text{H}_2\text{O}) = 20 \mu\text{bar}$  and an electron flux of  $9000 \text{ e}/\text{\AA}^2\text{s}$ , the amorphous edges start to recrystallize. Recrystallization of thin amorphous areas also affects the surfaces normal to the incident electron beam as indicated by the inhomogeneous image contrast (Mildner et al. 2015). An FFT-analysis of the high resolution TEM images shows that the structure of the formed nanocrystals is consistent with the perovskite Pbnm structure, although some traces of other phases cannot entirely be excluded.

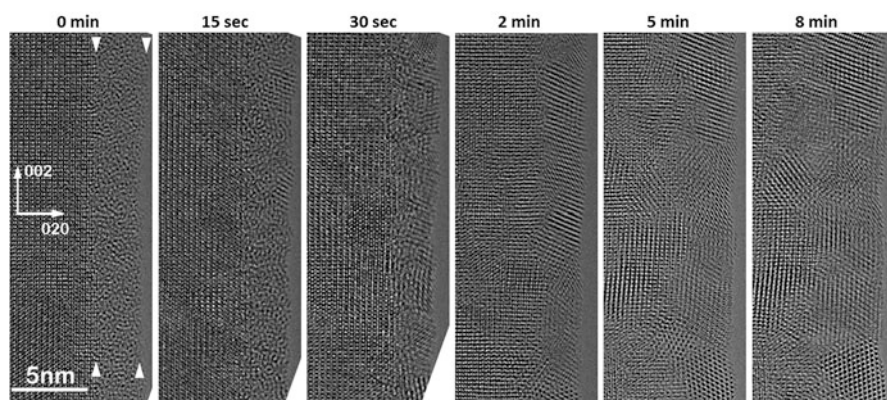


**Fig. 11.3** Time series of HRTEM images showing the recrystallization of an initially amorphous edge (marked with white arrowheads) of a PCMO film in water vapor at  $p_{\text{H}_2\text{O}} = 47 \mu\text{bar}$  and an electron flux of  $3.7 \times 10^4 \text{ e}/\text{\AA}^2\text{s}$ . The initial state is shown in the left image at  $t = 0 \text{ min}$

In order to better understand the influence of electron flux and partial water pressure on the recrystallization process we have performed several experiments observing recrystallization at different pressures and electron fluxes. We have recorded movies with a frame rate of 1 s to detect the appearance of first nanocrystals in the amorphous area. The specimen was kept out of the electron beam during the beam current setting. The results of these experiments are depicted in Fig. 11.4. The onset time for the recrystallization drops nearly exponentially with an increase of electron flux. Such an approximate dependence is expected according to the Butler-Volmer (11.7), if the reaction is driven by an electric potential which increases proportional to the electron flux (see Sect. 11.4).

Post-reaction EELS of the recrystallized areas has been performed at the Mn L-edge in high vacuum at 80 kV beam energy. The ratio of the integral Mn L<sub>3</sub>- and L<sub>2</sub>-edge intensities can be interpreted as a measure of the Mn valence state. Depending on beam flux, a systematic oxidation of the surficial Mn species in 5.5 μbar water vapor in contrast to a reduction in 47 μbar is observed. Figure 11.5a summarizes the results of the differently treated sample areas. The intensity ratios

**Fig. 11.4** Dependence of the onset time for recrystallization of an initially amorphous PCMO edge on the beam current

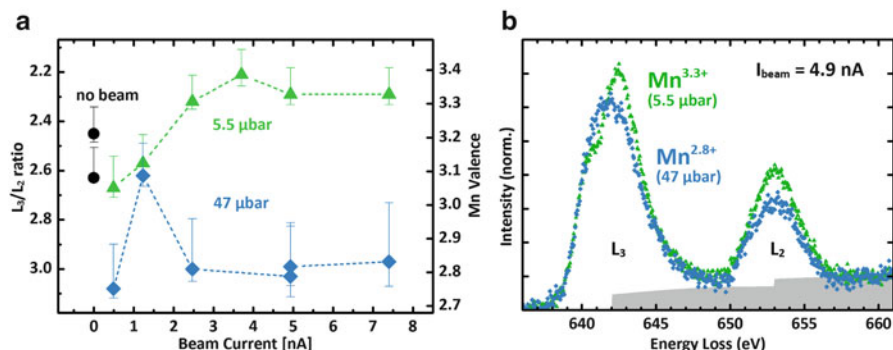
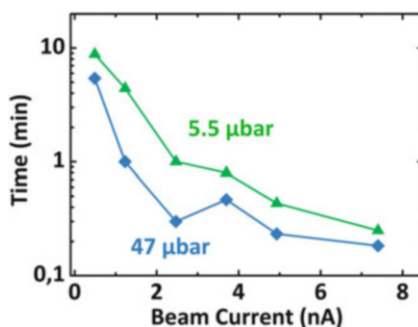


**Fig. 11.5** EELS of the PCMO sample at Mn L-edge after exposure to the electron beam in water vapor. Beam flux-dependent recrystallization leads to oxidation (5.5 μbar) or reduction (47 μbar) of the Mn surface species, shown by the Mn L<sub>3</sub>/L<sub>2</sub>-ratio (a). Examples for spectra of oxidized/reduced areas are given in (b)

have been translated into Mn valence state using the relationship found by Varela et al. for  $\text{La}_{1-x}\text{Ca}_x\text{MnO}_3$  powders (Varela et al. 2009). Figure 11.5b shows an example of spectra, which have been corrected for the power-law pre-edge background and normalized to unity at 658–661 eV. The energy has been calibrated according to X-ray absorption spectra of PCMO thin film samples (Mierwaldt et al. 2014) so that the  $L_2$ -edge is at 653 eV. The Hartree–Slater background model taken from Gatan Digital Micrograph is indicated by the filled grey curve. The two non-illuminated areas (black dots in Fig. 11.5a) exhibit a mean Mn valence below the expected value of 3.3+ due to the reduced amorphous surface layer. Recrystallization driven by a beam of 2.5 nA or more in 5.5  $\mu\text{bar}$  water vapor leads to oxidation of the surficial Mn to roughly 3.3+ matching the expectation for stoichiometric PCMO. Sample oxidation is likely to be driven by the positive beam induced surface potential. In contrast, illumination in 47  $\mu\text{bar}$  nominally reduces the Mn valence to roughly 2.8+. This reduction is consistent with other observations of surface/subsurface reduction of Mn valence in a  $\text{H}_2\text{O}$  pressure range between 13 and 100  $\mu\text{bar}$  under oxygen evolution conditions (Mierwaldt et al. 2014; Raabe et al. 2012). Whether it is intrinsically related to the active non-equilibrium state during oxygen evolution or it is driven by acidic conditions due to the increasing proton production during oxygen evolution at higher water partial pressure cannot be clarified at present.

### 11.3.3 *Oxygen Evolution at Manganite Electrodes Visualized by Sacrificial Reactions*

Electrochemical gas-phase reactions at solid electrode surfaces can be studied by using sacrificial agents which allow for monitoring electrochemical activity of the electrode via the induced growth of a solid phase on active areas. Raabe et al. (2012) presented an ETEM study of an oxygen evolution catalyst in a gas mixture of 1 mbar He with 0.01 mbar  $\text{H}_2\text{O}$  and a small amount of  $\text{SiH}_4$ . Electron beam driven  $\text{SiO}_{2-x}$  growth was observed at active crystalline edges of  $\text{Pr}_{1-x}\text{Ca}_x\text{MnO}_3$  ( $x=0.32$ ) (see Fig. 11.6) and interpreted as a direct solid state indicator for electro-catalytic activity for electrochemical water splitting and oxygen evolution.

The authors can exclude direct  $\text{SiH}_4$  oxidation via reaction with  $\text{H}_2\text{O}$ ,



or via deoxygenation of PCMO, since  $\text{SiO}_{2-x}$  growth is absent under the electron beam at inactive PCMO edges, such as amorphous areas (see Fig. 11.6h, i) or at negative applied potentials. The electro-catalytic  $\text{O}_2$  evolution

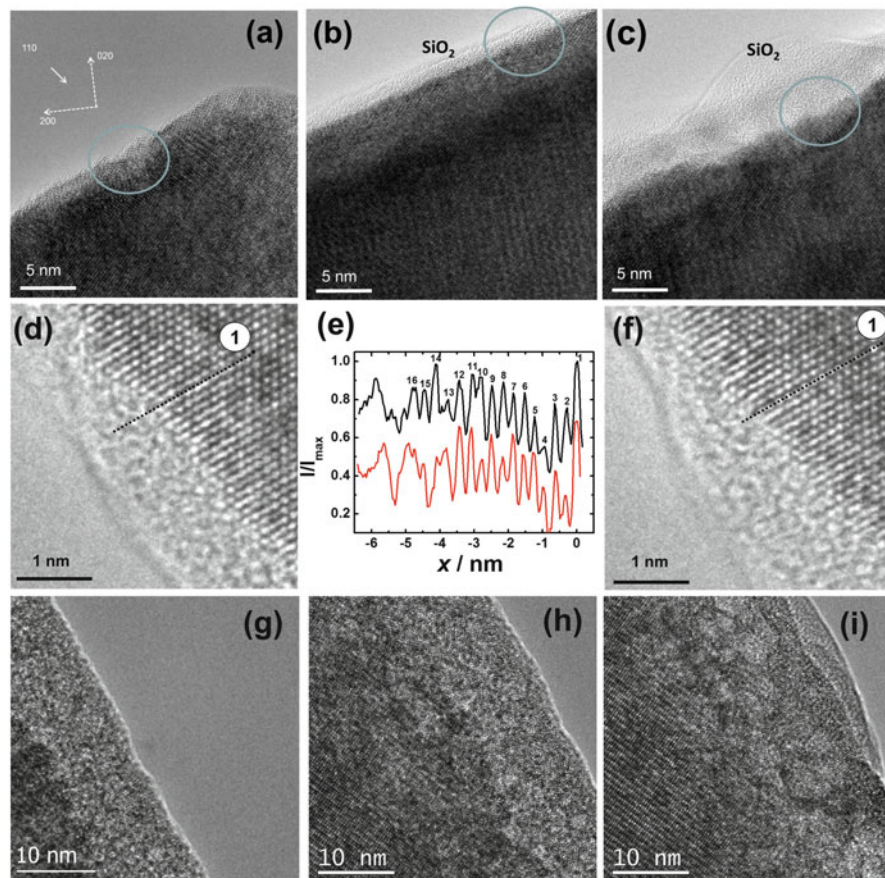
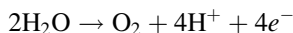
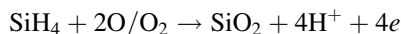


**Fig. 11.6** ETEM study of crystalline PCMO ( $x=0.32$ ) in contact with a He/H<sub>2</sub>O mixture ( $p(\text{H}_2\text{O}) \approx 0.13$  mbar) with small amounts of SiH<sub>4</sub> under electron flux of  $5 \times 10^4 \text{ e}^-/(\text{\AA}^2\text{s})$ . (a) HRTEM image acquired in high vacuum showing the pristine state of a crystalline edge on [001] axis. The same section as in (a) after injecting the gas mixture is shown in (b) 20 s and (c) 70 s after start of the electron beam stimulation. The growth of an amorphous SiO<sub>2-x</sub> layer indicates oxygen evolution activity. The grey circle is a marker for a specific edge location. (d, f) Show high-resolution TEM images of another area of the sample on [201] axis after 300 s and 310 s of electron beam exposure in H<sub>2</sub>O and resulting SiO<sub>2-x</sub> coverage. (e) Intensity modulation along the same line depicted in (d, f). The first atomic column of this line is labeled as “1.” (g, h) demonstrates the interplay between catalysis and corrosion and is used to analyze the catalytic TON (see text). (g–i) Absence of SiO<sub>2-x</sub> growth at an amorphous PCMO edge under the same conditions leading to SiO<sub>2-x</sub> growth at crystalline PCMO edges. (g) Virgin state of the amorphous sample edge in vacuum. (h, i) Morphology changes of that edge 40 and 160 s after start of electron beam stimulation, respectively. Parts of the figure have been published in Figs. 3 and S4 in Raabe et al. (2012)



and the related  $\text{SiO}_{2-x}$  growth via reaction with atomic or molecular oxygen



is visible by the increase of the O,  $\text{O}_2$ , and  $\text{H}_2$  mass signals on time scales of minutes after shifting the electron beam to a catalytically active sample edge (Figure S8 in the Supplemental Material of Raabe et al. 2012).

All experiments involving  $\text{H}_2\text{O}/\text{SiH}_4$  at catalytic edges show a strong slowing down of the  $\text{SiO}_{2-x}$  growth with increasing  $\text{SiO}_{2-x}$  thicknesses, which stops above a thickness of approximately 5–10 nm. We assume that after full coverage,  $\text{SiO}_{2-x}$  forms a diffusion barrier for the migration of the gas species. In addition, there is a slow transformation of crystalline PCMO into amorphous oxygen deficient PCMO at the PCMO- $\text{SiO}_{2-x}$  interface (Fig. 11.6d, f). The study of the interplay between the rates of  $\text{SiO}_{2-x}$  growth and PCMO amorphization thus allows for the analysis of the competition between catalysis and corrosion and thus for an estimate of the TON under such conditions. The line profiles in Fig. 11.6e taken from Fig. 11.6d, f show the change from a periodical oscillation (half  $b$ -lattice parameter  $b/2 = 0.29$  nm) to a disordered oscillation, indicating the crossover from well-crystalline PCMO to corroded amorphous PCMO followed by  $\text{SiO}_{2-x}$ , respectively. The comparison of the transformation rate of amorphous PCMO at  $\approx 1.8$  nm/min with the growth rate of  $\text{SiO}_{2-x}$  at  $\approx 10$  nm/min at the same region indicates TON of about 10 under the specified ETEM conditions. Thus, reduction of the PCMO ( $x = 0.32$ ) is not a main source of oxygen for  $\text{SiO}_{2-x}$  formation.

### 11.3.4 Two Electrode Experiments in Gas Phase: Bias Control of Corrosion

The Nanofactory STM-TEM holder shown in Fig. 11.10a is an example of an electrical TEM holder which can provide control over electric potentials at TEM specimens and allow for the realization of two electrode experiments by using the STM tip as a counter electrode. In particular, control over sample potential emerging within the electron irradiated specimen area due to secondary electron emission is possible by applying a compensating electric potential to the sample. As an example, Fig. 11.7 shows an ETEM experiment in  $\text{He}/\text{H}_2\text{O}/\text{SiH}_4$  gas mixture with a water partial pressure of 0.013 mbar under electron exposure with  $10^4$   $e/(\text{\AA}^2\text{s})$  with and without potential control via the STM tip.  $\text{SiH}_4$  has been used as a sacrificial agent in order to visualize electrochemical oxygen evolution activity via the growth of  $\text{SiO}_2$  at active surface (see Sect. 11.3.3) (Raabe et al. 2012). In Fig. 11.7a, b, a Ca-rich PCMO ( $x = 0.95$ ) sample area is shown before and after electron irradiation in gas without contact to the STM tip. The beam induced potential results in a

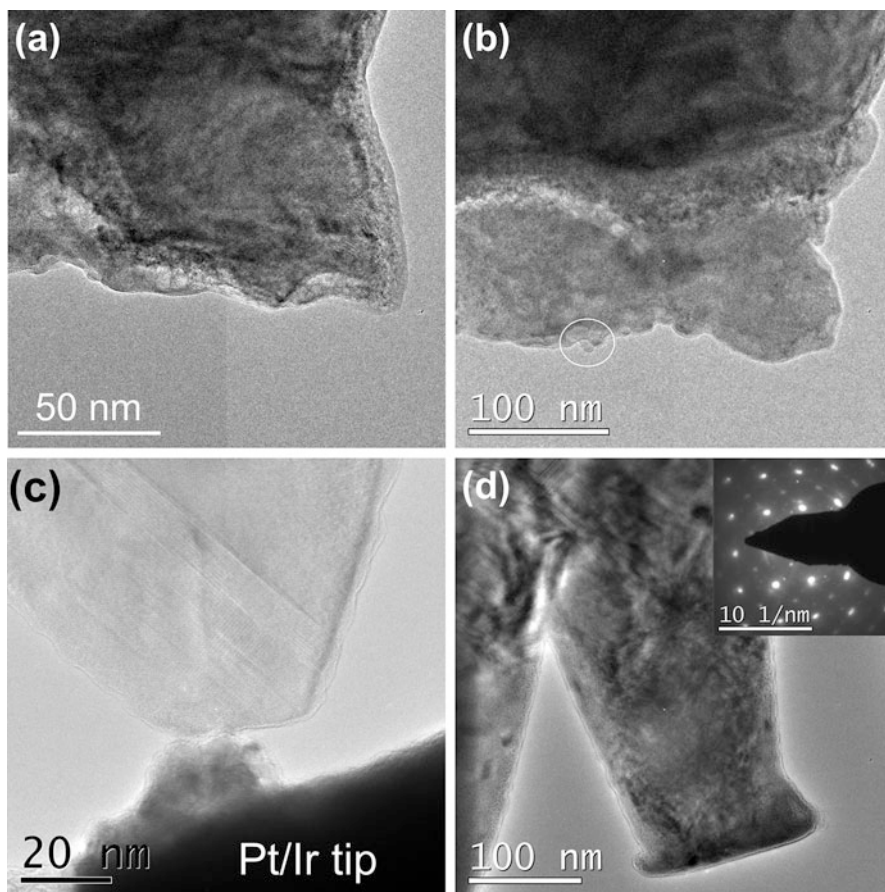


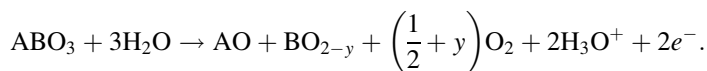
**Fig. 11.7** Two electrode electrochemical cell in the ETEM with PCMO  $x = 0.95$  working electrode and Pt/Ir as a counterelectrode. **(a)** Bright field overview TEM image of a crystalline PCMO grain in the virgin state. The corresponding diffraction pattern (*inset*) reveals the [001] zone axis. **(b)** Same area after 2 min irradiation with an electron flux of  $10^4 \text{ e}/\text{\AA}^2\text{s}$  in 0.013 mbar  $\text{H}_2\text{O}$ . A pronounced corrosion due to recrystallization and subsequent amorphization is observed. The *insets* show diffraction patterns of a recrystallized and an amorphous region, respectively. **(c)** Bright field overview TEM image of a crystalline PCMO edge in the [001] zone axis in the virgin state just before contact with the Pt/Ir tip. **(d)** State of the sample with  $-1 \text{ V}$  bias after an ETEM experiment under the same conditions as in **(b)**. No recrystallization or amorphization is observed and the perovskite structure of the electrode remains entirely intact as revealed by the corresponding diffraction pattern (*inset*) of the final state. See Figs. 5 and 6 in Raabe et al. (2012)

recrystallization followed by amorphization of the irradiated crystalline PCMO region in presence of water (Fig. 11.7b). EELS analysis of the amorphous area reveals a reduced Mn oxidation state compared to virgin areas which we interpret as a consequence of electrochemical reduction of PCMO generally proceeding at positive potentials of  $\approx 1 \text{ V}$ , i.e., the generation of oxygen vacancies results in an

intermediate recrystallization towards a non-perovskite structure and a subsequent amorphization (Fig. 11.7b).

The  $\text{SiO}_{2-x}$  growth which monitors oxygen evolution activity is strongly suppressed in Ca-rich samples because of their high corrosion instability under applied electrochemical conditions. Another area of the same sample under the same gas and electron illumination conditions but with an applied voltage of  $-1$  V is shown in Fig. 11.7c, d. The application of a negative potential at the sample in contact with the STM tip completely suppresses the corrosion observed without the application of an external potential (Fig. 11.7b). As can be seen in Fig. 11.7d, the initial perovskite structure is conserved. In addition,  $\text{SiO}_{2-x}$  growth is absent since the electrochemical oxygen evolution potential is seemingly not achieved under  $-1$  V bias. However, mechanical stress resulting from the contact between sample and tip leads to a slight modification of the sample shape (c.f. Fig. 11.7c, d). Our observation that the application of  $-1$  V can suppress the PCMO corrosion indicates that the beam induced potentials of the order of a volt can be compensated in a controlled manner by applied external potentials.

The observed electrochemical corrosion process of Ca-rich manganites in ETEM suggests an oxidation reaction at a positive beam induced potential as



Indeed, such an electrochemical decomposition is observed in ex situ cyclic voltammetry experiments using Ca-rich PCMO ( $x \geq 0.8$ ) electrodes in contact with liquid electrolytes. At  $\text{pH} = 7$ , the electrode corrosion is typically observed at an equilibrium potential in a range of  $V_0 = 0.2-0.35$  V versus standard hydrogen electrode (SHE) (Grygar 1999). Here, the perovskite decomposition leads to A-site cation dissolution in the liquid electrolyte which is absent in ETEM experiments in gas environment. In the presented two-electrode ETEM experiment, the application of a negative potential at the perovskite working electrode suppresses the anodic current from the gas species into the electrode. In contact with the Pt tip an overcompensation of beam-induced positive potential by an applied negative potential may even give rise to cathodic currents from the working electrode into the Pt working as a counter electrode.

### ***11.3.5 Two Electrode Experiments with Liquid Electrolytes: Lithium Intercalation***

One of the major challenges in gas phase electrochemistry is the absence of an electrolyte with sufficiently large ionic conductivity. Consequently, ion mass transport may represent a major reaction limiting step when comparing gas phase ETEM experiments at pressures below 20 mbar with real world electrochemical reactions



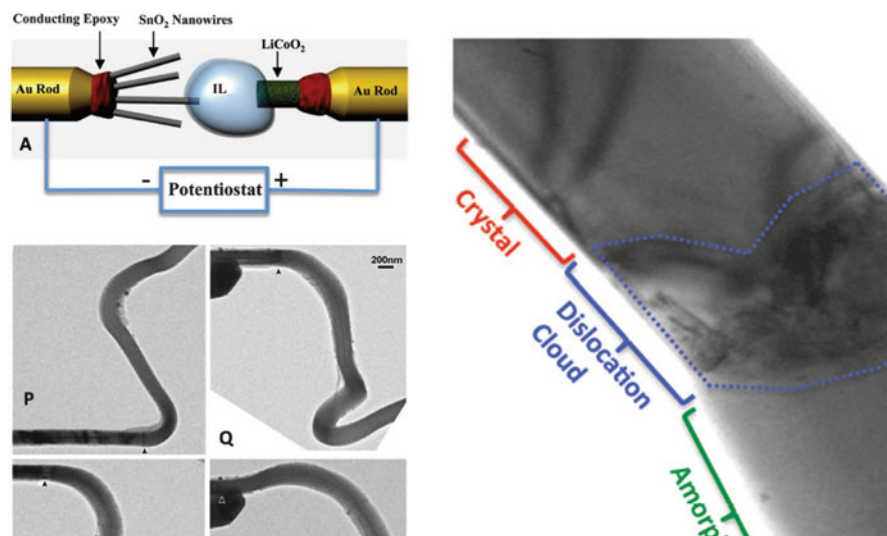
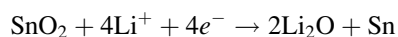


**Fig. 11.8** (a) Set-up of an in situ TEM electrochemical lithiation experiment of  $\text{SnO}_2$  nanowire electrodes using a  $\text{LiCoO}_2$  counter electrode and an ion liquid electrolyte with low vapor pressure. (P) to (S) are sequential high-magnification images showing the progressive migration of the reaction front, swelling, and the twisted morphology of the nanowire after the reaction front passed by. (G) TEM image showing the high density of dislocations that appeared at the reaction front. (Reproduced with permission The American Association for the Advancement of Science from J. Y. Huang et al. *Science* 330 (2010) 1515-1520)

with gaseous or liquid reactants. An important class of electrochemical in situ experiments was therefore carried out in recent years based on ionic liquid (ILE) (Huang et al. 2010; Zhong et al. 2011) and solid state  $\text{Li}_2\text{O}$  or carbon based electrolytes (Liu et al. 2012; Ebner et al. 2013; Zhong et al. 2013). The ionic liquid is a molten organic salt with very low vapor pressure, enabling its use in high vacuum ( $\approx 10^{-7}$  mbar) inside TEM's without differential pumping while still solvating and transporting Li ions effectively.

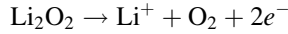
As an example, we summarize here an in situ TEM lithiation study of  $\text{SnO}_2$  nanowires which was presented by Huang et al. (2010); see Fig. 11.8. The nano-scale battery was arranged by mounting  $\text{SnO}_2$  nanowire electrodes, a  $\text{LiCoO}_2$  counter electrode and ILE based electrolytes in a Nanofactory STM-TEM holder (Fig. 11.10). Electrochemical lithiation takes place at negative potentials of the order of  $-3.5$  V. The lithium intercalation into  $\text{SnO}_2$  happens via a reaction front, where a moving dislocation cloud enables an enhanced Li mobility in the  $\text{SnO}_2$  phase resulting in a phase transformation from the crystalline  $\text{SnO}_2$  into a phase which contains nanocrystalline  $\text{Li}_x\text{Sn}$  and Sn particles embedded into an amorphous  $\text{Li}_2\text{O}$  phase, i.e.,



with  $\text{Li}_x\text{Sn}$  reaction intermediates. The volume change of the phase transformation gives rise to nanowire expansion and thus some twisting and bending during the

evolution of the reaction front through the nanowire. Discharging at positive potential does not affect the  $\text{Li}_2\text{O}$  matrix and thus is not fully reversible.

Another in situ TEM study of electrochemical oxidation of



shows that the reaction is charge-transfer limited since the low electronic conductivity of  $\text{Li}_2\text{O}_2$  gives rise to high overpotentials (Zhong et al. 2013).

## 11.4 Electron Beam Induced Electric Potentials

Electric potentials of a magnitude relevant for electrochemistry can be easily generated by inelastic scattering of high energy electrons incident on a thin TEM foil specimen which results in the emission of Auger electron, core electrons as well as secondary electrons (SE). Electron emission from a TEM specimen leaves hole carriers, i.e., positive charges, within the specimen. Thus, depending on the electric conductivity of the sample, positive charges can accumulate within the electron beam exposed specimen areas resulting in a positive electric potential. This potential, on the one hand, generates an energy barrier for subsequent electrons trying to escape from the sample, i.e., the emission rate decreases with increasing potential. On the other hand the positive potential attracts negative charges from grounding or the environment, which compensate the holes generated by SE emission. The induced sample potential thus depends sensitively on the primary electron flux as well as on the electric conductivity of the sample and electric contact conditions. The evolving steady state potential is thus governed by the balance of the emission,  $I_{\text{SE}}$ , and the neutralization,  $I_{\text{N}}$ , currents:

$$\frac{dQ}{dt} = I_{\text{SE}} + I_{\text{N}} = 0. \quad (11.10)$$

Even under low-dose conditions, where the effect of beam damage due to atomic displacements may be absent, beam induced electric potentials can have a major effect on the electrode/catalyst state. In the following we present a theoretical model of the beam induced potential in combination with experimental approaches for measuring it. Since SE emission is the predominant fraction of electron emission processes (Cazaux 2010), we restrict our calculation on that species in Sect. 11.4.1. A short discussion of possible charge neutralization sources is subject of Sect. 11.4.2. Furthermore, we introduce methods for measuring electron beam induced potentials in a TEM by using electrical holders in Sect. 11.4.3 and by using off-axis holography in Sect. 11.4.4.

### 11.4.1 Determination of Secondary Electron Emission Yields from Electron Transparent Thin Foils

Electron emission from a condensed matter sample involves two basic steps: First, the beam induced excitation of a specimen electron to energies above the ionization edge and, second, the propagation of the excited (hot) electron to the surface of the specimen. The former depends on materials properties. The latter considers scattering of the SE within the specimen and is also affected by the specimen geometry. Electron emission further depends on the beam induced potential which will be discussed later. These two steps form the basis for theoretical treatments of the secondary electron yield  $Y$ , which relates the emission current  $I_{SE}$  and the primary beam current through the sample  $I_P$  via  $Y = I_{SE}/I_P$ , in the literature (Cazaux 2010; Henke et al. 1979; Chung and Everhart 1974). In 1974 Chung and Everhart derived an equation applicable to macroscopic metallic samples (Chung and Everhart 1974) with thicknesses  $d$  much larger than the inelastic mean free path  $\lambda$  of generated SE in the material. We adapt the Chung–Everhart equation to TEM thin foils with  $d = \lambda$  by introducing the factor  $1 - \exp\left(-\frac{d}{\lambda(E)}\right)$  which takes into account the limitation of  $Y$  by the finite thickness.<sup>1</sup>

$$\frac{dY}{dE}(E, \phi) = 2 \cdot \frac{S(E)\lambda(E)}{4} \cdot F(E, \phi) \cdot \left[ 1 - \exp\left(-\frac{d}{\lambda(E)}\right) \right] \quad (11.11)$$

Equation (11.11) describes the energy distribution of emitted SE per incident electron current and unit time. The term  $F(E, \phi) = 1 - (E_F + \phi)/E$  depends on the work function  $\phi$ . It accounts for energy losses during the propagation of an SE excited to energies above the ionization edge,  $E > E_F + \phi$ , across the specimen surface to vacuum. In other words, it reflects the escape probability of an excited SE with energy  $E$ . SE energies  $E$  are given relative to the bottom of the conduction band.  $S(E) = C_Y(E_P)/(E - E_F)^2$  denotes the number of electrons excited to an energy interval  $E + dE$  per primary electron and unit path.  $C_Y$  is a material specific constant and  $E_P$  denotes the energy of the primary electrons.  $C_Y$  can be obtained either theoretically (Streitwolf 1959) or in a semi-experimental way using common rate equations on the basis of scattering cross sections

<sup>1</sup> In the derivation of (11.10), we approximate the term  $\exp(-d/\lambda \cos \theta)$  with  $\exp(-d/\lambda)$  (c.f. (11.5) in Chung and Everhart 1974) when integrating over the allowed angular range of SE trajectories. In doing so, we effectively underestimate by a small amount the contribution to the yield of those secondaries with energies just above the work function. Numerical comparisons show that this approximation affects the yield spectrum  $dY/dE$  at most by about 1 %.

$$\frac{dn_{\text{ion}}}{dt dx} = n_s \cdot \sigma_{\text{ion}}(E_P) \cdot \frac{dn_P}{dt} . \quad (11.12)$$

Equation (11.12) relates the number of ionization processes per unit time and unit primary electron path  $dx$  with the specimen atomic density  $n_s$ , the primary particle current  $\frac{dn_P}{dt}$  and the material specific ionization cross sections  $\sigma_{\text{ion}}$ . Experimental values of  $\sigma_{\text{ion}}$  are available in literature and online databases (<http://dbshino.nifs.ac.jp>). For PCMO it amounts to  $\sigma_{\text{ion}}(E_P) = 3 \times 10^{-23} \text{ m}^2$  at  $E_P = 300 \text{ keV}$ . According to (11.12)  $n_s \cdot \sigma_{\text{ion}}(E_P)$  gives the number of ionization processes per primary electron and unit path which is equal to the total number of electron excitations  $S(E)$  with final energies  $E > E_F + \phi$ .

$$n_s \cdot \sigma_{\text{ion}}(E_P) = \int_{E_F + \phi}^{\infty} S(E) dE = \frac{C_Y(E_P)}{\phi} . \quad (11.13)$$

We calculate (11.13) for PCMO ( $x = 0.35$ ) using  $n_s = 8.76 \times 10^{28} \text{ m}^{-3}$ ,  $\phi = 4.9 \text{ eV}$  (Reagor et al. 2004),  $E_F = 1.84 \text{ eV}$  calculated via  $E_F = \frac{\hbar^2}{2m} (3\pi^2 n_e)^{\frac{2}{3}}$ , where  $n_e = (1 - x)/V_{\text{SC}}$  with hole doping level  $x = 0.35$  and the simple cubic unit cell volume  $V_{\text{SC}} \approx (3.8 \text{ \AA})^3$ .

Finally, we calculate the inelastic mean free  $\lambda(E)$  path of the generated SE with the semi-empirical expression given by Seah and Dench (1979) for inorganic compounds

$$\frac{\lambda(E)}{a} = 2170(E - E_F)^{-2} + 0.72(a(E - E_F))^{\frac{1}{2}}, \quad (11.14)$$

where  $a$  denotes the monolayer thickness (for PCMO  $a = 0.38 \text{ nm}$ ). Inserting (11.13) and (11.14) in (11.11) and integration over the kinetic energy of the SE gives a total secondary electron yield  $Y_0$

$$Y_0 = \int_{E_F + \phi}^{\infty} \frac{dY}{dE} dE = 0.0034. \quad (11.15)$$

A positive potential  $V$  arising from SE emission creates a barrier for ionized electrons that reduces their escape probability. This effect can be easily included in (11.11) by increasing the effective work function to  $\phi + eV$ :

$$\frac{dY}{dE}(E, \phi, V) = 2 \cdot \frac{S(E)\lambda(E)}{4} \cdot \left(1 - \frac{E_F + \phi + eV}{E}\right) \cdot \left[1 - \exp\left(-\frac{d}{\lambda(E)}\right)\right] \quad (11.16)$$

In Fig. 11.9a the energy distribution  $\frac{dY}{dE}(E, \phi, V)$  has been calculated for different potentials  $V$ . The total yield as a function of potential  $V$  is shown in Fig. 11.9b.

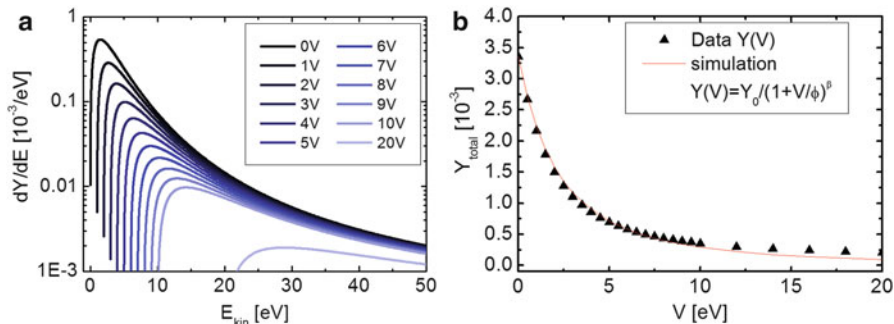


**Fig. 11.9** The secondary electron yield depending on the beam induced electric potential  $V$  calculated according to (11.16). (a) The energy distribution of emitted SE per primary electron for different values of  $V$  and (b) the total yield as a function of  $V$  and a power law fit (red line) giving rise to the equation (11.17)

It reveals a rapid decrease of  $Y(V)$  following a power law  $Y(V) = Y_0 / \left(1 + \frac{V}{\phi}\right)^\beta$  with the exponent  $\beta \sim 2.2$  which leads to a self-limitation of the evolving potential. We define  $v \equiv \frac{V}{\phi}$ , write  $Y(V) = I_{SE}(V)/I_P$ , and obtain  $I_{SE}(v) = \frac{Y_0 I_P}{(1+v)^\beta}$ . In the stationary state emission currents and neutralization currents balance,  $I_N(v) = I_{SE}(v)$ . Describing  $I_N(V)$  as a function of the sample resistance  $R(V)$  yields

$$v(1+v)^\beta = \frac{Y_0 I_P R(V)}{\phi}. \tag{11.17}$$

Thus, the steady state potential strongly depends on the sample resistance which governs the neutralization currents.

### 11.4.2 Neutralization Currents

In TEM samples with low-resistive (metallic-like) pathways to ground the neutralization of holes generated within the electron irradiated specimen occurs via grounding currents. The high grounding currents may provide an almost entire compensation of generated holes and limit the evolving potential to vanishingly small values. However, grounding currents in cross section TEM samples of electrode/electro-catalysts sensitively depend on the chosen support material.

A second contribution to charge neutralization may be provided by a gaseous environment in the TEM similar to observations in SEM (Meredith et al. 1996; Moncrieff et al. 1978). Ionization of gas species or rather secondary electron emission from gas species may provide negative charges for compensating holes within the TEM specimen. However, simple calculations considering the cross sections for electron attachment to gas species (here  $H_2O$  and He) as well as

electron emission from gas species yield negligible neutralization currents on the order of 1 fA at conventional ETEM gas pressures. To give an example, a He pressure of 0.3 mbar using 300 keV electrons with a primary beam current density of  $10^4 \text{ e}/\text{\AA}^2 \text{ s}$  results in a negative charge generation yield of  $10^{-8} - 10^{-6}$  per primary electron which is at least four orders of magnitude lower than the total yield per primary electron in solid samples. Thus, we conclude that even in high resistive samples the grounding current is the primary charge compensation mechanism in TEM thin foils.

### 11.4.3 Direct Measurement of Beam Induced Potentials

In this section we show two experiments in the TEM that support the theoretical considerations above. First, we show an experiment where we measure the sample resistance using an electrical biasing TEM holder equipped with a piezo-driven PtIr-STM tip (Fig. 11.10a). Additionally, we show electron holography experiments which reveal a phase shift of electron waves traversing the specimen and the vacuum nearby which carries information about the electric potentials within the specimen.

With an electrical biasing TEM holder we measure I-V characteristics of a PCMO/MgO cross section TEM sample (see Fig. 11.10). We obtain a resistance that strongly depends on the sample potential. It can be adequately simulated with a Frenkel–Poole conduction mechanism (Fig. 11.10b). By fitting the measured  $R(V)$  curve via a Frenkel–Poole  $R(V)$  dependence, we obtain  $R(V_0) \cong 1 \text{ M}\Omega$ . Depending on sample preparation and surface adsorbents, a resistance of MgO lamellas of similar geometry of up to  $R(V \rightarrow 0) \cong 67 \text{ G}\Omega$  has been measured.

Removing the tip from the specimen and interconnecting a 200 T $\Omega$  resistance leads to a development of a positive electric potential of several volts under electron irradiation (Fig. 11.10d), depending on primary beam current and gas pressure. The induced potential evolving in 5  $\mu\text{bar}$  water vapor pressure is higher than in vacuum. This is a surprising result since a gaseous environment is commonly considered to reduce beam induced charging effects. However, the combination of water vapor presence and electron exposure turns out to remove carbon contamination on the specimen surface and, thus, increases the leakage resistance.

In the following, we provide a test of the results obtained from the balance of current (11.10) and the estimated yield (11.15) by the measurement of the time evolution of the sample voltage (Fig. 11.10d). In this experimental configuration, the connection to ground is severed ( $I_N \ll I_{SE}$  for  $V < 10 \text{ V}$  and  $I_P = 5.4 \text{ nA}$ )<sup>2</sup> and the balance of currents reads simply

<sup>2</sup>Due to the 200 T $\Omega$  input resistance  $I_N(10 \text{ V}) \sim 50 \text{ fA} \ll I_{SE}(10 \text{ V}) \sim 1.5 \text{ pA}$  for  $I_P = 5.4 \text{ nA}$ . Calculation of  $I_{SE}$  via  $I_{SE}(v) = (Y_0 I_P)/(1+v)^\beta$ . With increasing  $V$ ,  $I_N$  increases to values of more than 10 % of  $I_{SE}$  and  $I_N \ll I_{SE}$  is not fulfilled.

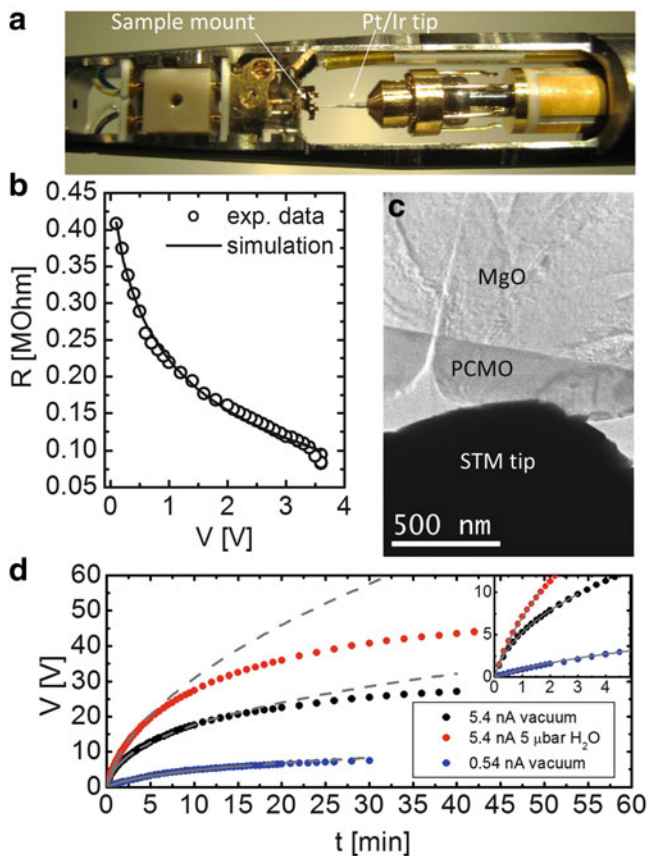


**Fig. 11.10** Sample resistance and potential built-up measured in a cross section TEM sample cut from a PCMO thin film sample on insulating MgO substrate using a TEM holder equipped with a STM tip. (a) A photo of the electrical biasing holder showing the sample support and the piezo-driven STM tip. (b) The measured sample resistance as a function of applied potential without electron irradiation. (c) TEM image depicting the PCMO/MgO TEM sample in contact with a PtIr STM tip. (d) The measured electric potential as a function of time after starting electron exposure of a PCMO area with a diameter of 300 nm with a primary beam current through the sample  $I_P = 0.54$  nA (blue) and  $I_P = 5.4$  nA in vacuum (black) and in water pressure of  $p_{\text{H}_2\text{O}} = 5$   $\mu\text{bar}$  (red). The potential is measured using an electrometer with an internal resistance of 200 T $\Omega$ . For this configuration, the measured increase of the potential with time,  $V(t)$ , is fitted (grey lines) in the range  $0 < V < 10$  V for ( $I_P = 5.4$  nA) and  $0 < V < 6$  V for ( $I_P = 0.54$  nA) with a capacitor model described in the text below according to (11.22). This model is valid in a voltage range, where  $I_N \ll I_{SE}$ . The resulting time constants are summarized in Table 11.1

$$\frac{dQ}{dt} = I_{SE} = Y(V)I_P, \quad (11.18)$$

implying that the object will keep charging up, although at a rate that decreases with time. For a floating metallic object, each  $dQ$  of charge added or removed from its

**Table 11.1** Results of fitting  $V(t)$  data presented in Fig. 11.10d with (11.22) and (11.21)

Data (presented in Fig. 11.10c)	$\tau$ (s)	$\alpha$	C (pF)
Blue data [ $I_P = 0.54$ nA, $p \sim 10^{-7}$ mbar]	73.62	0.308	90
Black data [ $I_P = 5.4$ nA, $p \sim 10^{-7}$ mbar]	9.18	0.363	95
Red data [ $I_P = 5.4$ nA, $p \sim 5 \times 10^{-3}$ mbar]	12.63	0.513	92

interior changes its potential, measured with respect to infinity, by an amount  $dV$ , where  $C = dQ/dV$  is the self-capacitance of the body. Therefore, we can write

$$dV/dt = Y(V)I_P/C, \quad (11.19)$$

which can be solved in closed form if we take the  $Y(V)$  as discussed above

$$dv \cdot (1 + v)^\beta = \alpha \cdot dt/\tau, \quad (11.20)$$

where we reintroduce  $v = V/\phi$  and define

$$\tau = \alpha \cdot \phi \cdot C / (Y_0 \cdot I_P) \quad \text{with} \quad \alpha = \frac{1}{\beta + 1}, \quad (11.21)$$

Giving

$$v(t) = -1 + \left(1 + \frac{t}{\tau}\right)^\alpha. \quad (11.22)$$

Equation (11.22) is used as a model to fit the data shown in Fig. 11.10d. The results of the fit are summarized in Table 11.1. The determination of the specimen capacity via (11.21) gives reasonable values. Minor variations of the obtained capacity presumably result from variations of the specimen thickness at the different sample regions where the measurements shown in Fig. 11.10d are performed. The deviations between the measured and fitted curve at  $V \geq 10$  V are due to the increasing contribution of residual leakage currents (see Footnote 2). These observed deviations from a capacitive charging approximation is important, since it indicates that the beam induced potential tends to saturates at high enough potential values even for insulating samples.

The measurement of the potential-dependent sample resistance shown in Fig. 11.10b provides additional information for a semi-experimental determination of the beam induced potential via equation (11.17). We use the  $R(V)$  characteristics of a TEM sample cut from the MgO catalyst support to simulate the implicit expression (11.17) for different values  $v$  and  $I_P$ . The result is shown in Fig. 11.11. The higher the primary current  $I_P$  is the higher the emission current  $I_{SE}$  and the higher the induced positive potential. The value of the steady state potential for the different parameters  $v$  and  $I_P$  are labeled with open circles.



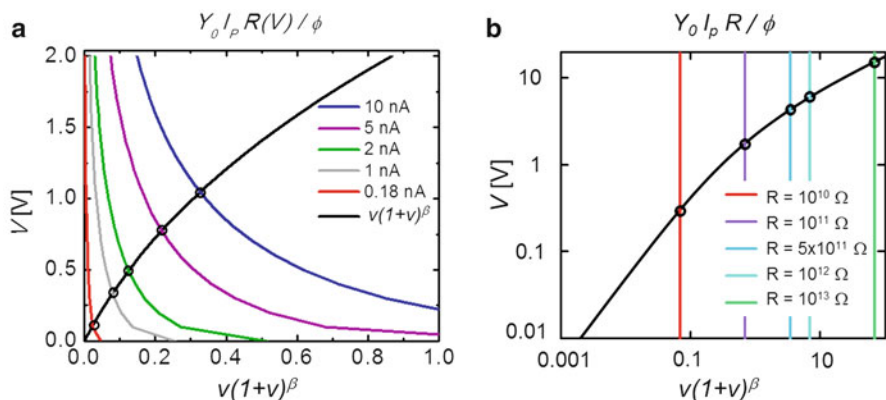


**Fig. 11.11** Graphical solution of (11.17) by plotting the left side (lower axis) and the right side (upper axis) for different beam and sample parameter. **(a)** Sample potential  $V$  for the measured Frenkel–Poole like resistance of a MgO catalyst support for different primary beam currents. Limiting cases are  $R(V \rightarrow 0) = 6.7 \times 10^{10} \Omega$  and  $R(V = 10 \text{ V}) = 4 \times 10^9 \Omega$ . **(b)** Sample potential  $V$  for a constant beam current of  $I_p = 10 \text{ nA}$ , and different sample/contact resistances of ohmic type. Materials parameters are chosen for the manganite PCMO with total scattering yield of  $Y_0 = 0.0034$  and work function  $\phi = 4.9 \text{ eV}$

We have to note here that the total resistance of a TEM lamella with respect to ground does not only depend on the specific resistance of the involved materials and the involved contact/interface resistances. There can be orders of magnitude changes due to surface defects and contamination which depend on the TEM sample preparation as well as on the sample cleaning procedure and the vacuum conditions of the ETEM. For example, from the bulk resistivity of MgO of  $\rho = 10^{15} \Omega\text{cm}$  (Cazaux et al. 1991) one would expect a total resistance of  $\sim 10^{20} \Omega$  for a typical FIB cut TEM lamella of dimensions of 50 nm thickness, 1  $\mu\text{m}$  width, and 1 mm length. Our measured resistances are in the M $\Omega$  to G $\Omega$  range and can even vary during an experiment due to change in surface contamination.

### 11.4.4 Measurement of Beam Induced Potentials by Off-Axis Electron Holography

Off-axis electrons holography allows for reconstruction of the phase and the amplitude of the electron wave traversing the TEM specimen, information that is lost in conventional TEM. Electric potentials  $V(\mathbf{r})$  influence the phase of the beam electron wave propagating in  $z$  direction and lead to a phase shift  $\Delta\phi$  of

$$\Delta\phi(x, y) = C_E \int_{-\infty}^{+\infty} V(x, y, z) dz. \quad (11.23)$$

The constant  $C_E$  depends on the kinetic energy of the beam electrons. For 300 keV electrons  $C_E = 6.53 \text{ rad V}^{-1} \mu\text{m}^{-1}$ .

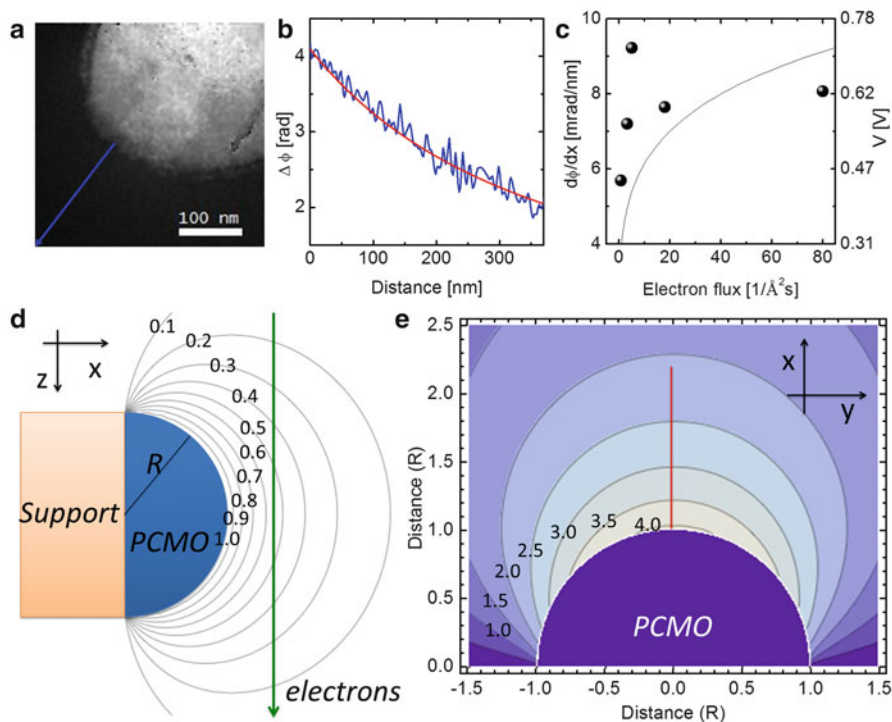
The creation of a hologram is based on the separation of an electron wave into two parts via a positively charged metal wire before passing the specimen. One part of the wave passes through the sample and suffers a phase shift due to the electric field present within and around the (charged) object. The other part of the wave passes through vacuum, i.e., a region of space where, ideally, no electric fields are present. The coherent superposition of the two portions of the electron wave produces an interference pattern—the hologram. A reconstruction of the hologram via numerical methods allows the extraction of the phase shift, which enables us to estimate the potential.

Figure 11.12a shows the phase image of a PCMO ( $x = 0.35$ ) sample region on MgO substrate during irradiation with an electron flux of  $80 \text{ e}^-/\text{\AA}^2\text{s}$ . In order to get an estimate of the surface potential we analyze the phase shift at the PCMO/vacuum interface on the vacuum side. Inside the specimen the phase shift of the beam electrons is governed by the mean inner potential arising from the magnetic properties and the charge density distribution of specimen electrons and atomic nuclei. Figure 11.12b presents the line profile of the phase shift along the blue arrow. In order to get a rough order-of-magnitude estimate of the surface potential, we assume a hemispherical specimen shape with radius  $R$  kept at a constant surface potential  $V_S$  with respect to a grounded plane (see Fig. 11.12a). The solution of the Laplace equation for this problem, computable analytically as a series of Legendre Polynomials, yields the electrostatic potential in the vacuum area outside the object. By integrating this potential along the beam path ( $z$ -axis), and focusing on the region just outside the object, we obtain the following approximation for the phase gradient:

$$\frac{d\Delta\phi(R)}{dx} \cong -2C_E V_S. \quad (11.24)$$

From Fig. 11.12b we get a phase shift gradient of  $\nabla\phi = 8 \text{ mrad/nm}$  at electron flux of  $80 \text{ e}^-/\text{\AA}^2\text{s}$  which yields an electric potential of  $V \sim 0.6 \text{ V}$  (based on (11.24)). The phase shift gradient and accordingly the surface potential increases with increasing electron flux as shown in Fig. 11.12c.

A more sophisticated model for the determination of beam induced potentials from electron holography experiments based on more realistic approximations is given in (Mildner et al. 2015).



**Fig. 11.12** (a) Phase image of a roughly semi-circular PCMO ( $x = 0.35$ ) region. (b) Phase shift profile in vacuum along the blue line in (a). (c) Phase shift gradient at the PCMO/vacuum edge as a function of the primary electron flux; the thin line represents a simulation of the data based on the balance of currents (see Sect. 11.4.3 and Fig. 11.11). (d) Simplified geometry of the PCMO region modeled as an equipotential hemisphere generating an electrostatic potential in its surroundings (potential contours in fractions of the surface potential). (e) Phase shift (contours in rad) corresponding to the geometry in (d); the phase profile along the red line is shown as the red curve in (b)

## 11.5 Summary and Conclusions

We have shown that in situ TEM experiments in gas and liquid environments can give insights into many important aspects of electrode and electro-catalyst behavior during electrochemical reactions. The change in Gibbs energy of the catalyst surface in contact with gas or liquid species can give rise to the development of new states of electrochemical equilibrium with modified surface and interface atomic and electronic structure. One example is the formation of oxide nanocrystals during oxidation and reduction of an oxygen deficient amorphous region in the transition to the new electrochemical equilibrium structure in contact with water vapor.

Crucial for the understanding of electrode and catalyst behavior are studies of active states in redox experiments. The study of active states at manganite

perovskites during water splitting exhibits a reduction of the formal valence state from  $\text{Mn}^{3.3+}$  to  $\text{Mn}^{2+}$  due to the formation of surface oxygen vacancies. Slowly enough evolving transient states of catalysts, electrodes and reactions zone can enable a deeper understanding of the nature of barriers. Stranski–Krastanov-like formation of metal-oxide islands on a wetting layer during oxidation of the metal and the moving interaction zone during lithiation of battery electrodes with a high density of dislocations are examples showing a rich world of structures which are not present in the initial and final state of the chemical transformation. Active sites and zones have been demonstrated in surface oxidation which nucleates at surface steps as well as at catalytic activity at crystalline edges of manganites which is absent at amorphous areas. The use of sacrificial agencies can be of high value for monitoring gas phase electrochemical reactions by the growth of a solid layer, as was demonstrated by using silane for monitoring oxygen evolution.

While such in situ experiments show fascinating atomic scale dynamics under different conditions, the realization of well-defined electrochemical studies is challenged by several effects. First of all, even below the threshold of beam damage under vacuum conditions, the electron beam induced charging of semiconducting or insulating electrodes or catalyst supports can have a strong effect on the catalyst state, since the evolving potentials easily can access values, where electrochemical reactions are possible. Consequently, the control of beam induced potentials and the application of well-defined external potentials is absolutely necessary in order to study electrochemistry under controlled conditions. An additional challenge in ETEM electrochemistry experiments is the establishment of clean chemical environments, clean sample surfaces and understanding the effects of thin TEM lamella preparation. Measurement of reaction products by mass spectrometry of the gas flowing through in the sample chamber is only possible by accumulating the small amounts of chemical reaction products over times of tenth of minutes. Whereas qualitative analysis of change of gas composition is possible, quantification of reaction products and combination to measured quantities of transferred charge seems to be far of reach at present, due to beam effects and limited measurement sensitivity for chemical species.

One of the most promising developments in ETEM electrochemistry is the application of well-defined external potential by a set of electrical sample holders. Various options have been developed in recent years which involve two-electrode geometries based on the Nanofactory STM holder as well as two and three electrode geometries which are accessible by microelectromechanical systems solutions.

**Acknowledgements** We are grateful for the support of Sadegh Yazdi and Takeshi Kasama from the Center for Electron Nanoscopy, Technical University of Denmark, for the acquisition of holography data presented in Fig. 11.12. Financial support is acknowledged by the DFG through the SFB1073/project C02.

## References

- R. Arrigo, M. Hävecker, M.E. Schuster, C. Ranjan, E. Stotz, A. Knop-Gericke, R. Schlögl, *Angew. Chem. Int. Ed.* **52**, 11660 (2013)
- S. Blomberg, M.J. Hoffmann, J. Gustafson, N.M. Martin, V.R. Fernandes, A. Borg, Z. Liu, R. Chang, S. Matera, K. Reuter, E. Lundgren, *Phys. Rev. Lett.* **110**, 117601 (2013)
- J. Cazaux, *Ultramicroscopy* **110**, 242 (2010)
- J. Cazaux, K.H. Kim, O. Jbara, G. Salace, *J. Appl. Phys.* **70**, 960 (1991)
- L.Y. Chang, A.S. Barnard, L.C. Gontard, R.E. Dunin-Borkowski, *Nano Lett.* **10**, 3073 (2010)
- S. Chenna, P.A. Crozier, *Micron* **43**, 1188 (2012)
- M. Chung, T. Everhart, *J. Appl. Phys.* **45**, 707 (1974)
- J.F. Creemer, S. Helveg, P.J. Kooyman, A.M. Molenbroek, H.W. Zandbergen, P.M. Sarro, *J. of Microelektromechanical Systems* **19**, 254 (2010)
- M. Ebner, F. Marone, M. Stampanoni, V. Wood, *Science* **342**, 716 (2013)
- T. Grygar, *J. Solid State Electrochem.* **3**, 412 (1999)
- P.L. Hansen, J.B. Wagner, S. Helveg, J.R. Rostrup-Nielsen, B.S. Clausen, H. Topsøe, *Science* **295**, 2053 (2002)
- T.W. Hansen, J.B. Wagner, R.E. Dunin-Borkowski, *Mater. Sci. Technol.* **26**, 1338 (2010)
- S. Helveg, C. López-Cartes, J. Sehested, P.L. Hansen, B.S. Clausen, J.R. Rostrup-Nielsen, F. Abild-Pedersen, J.K. Nørskov, *Nature* **427**, 426 (2004)
- B.L. Henke, J. Liesegang, S.D. Smith, *Phys. Rev. B* **19**, 3004 (1979)  
<http://dbshino.nifs.ac.jp>
- J.Y. Huang, L. Zhong, C.M. Wang, J.P. Sullivan, W. Xu, L.Q. Zhang, S.X. Mao, N.S. Hudak, X.H. Liu, A. Subramanian, H. Fan, L. Qi, A. Kushima, J. Li, *Science* **330**, 1515 (2010)
- G.J. Hutchings, A. Desmartin-Chomel, R. Olier, J.-C. Volta, *Nature* **368**, 41 (1994)
- K.L. Kein, I.M. Anderson, N. De Jonge, *J. Microsc.* **242**, 117 (2011)
- X.H. Liu, J.W. Wang, Y. Liu, H. Zheng, A. Kushima, S. Huang, T. Zhu, S.X. Mao, J. Li, S. Zhang, W. Lu, J.M. Tour, J.Y. Huang, *Carbon* **50**, 3836 (2012)
- P. Meredith, A.M. Donald, B. Thiel, *Scanning Vol.* **18**, 467 (1996)
- D. Mierwaldt, S. Mildner, R. Arrigo, A. Knop-Gericke, E. Franke, A. Blumenstein, J. Hoffmann, Jooss, *Ch. Catalysts* **4**, 129 (2014)
- D.A. Moncrieff, V.N.E. Robinson, L.B. Harris, *J. Phys. D Appl. Phys.* **11**, 2315 (1978)
- S. Raabe, D. Mierwaldt, J. Ciston, M. Uijtewaal, H. Stein, J. Hoffmann, Y. Zhu, P. Blöchl, C. Jooss, *Adv. Func. Mat.* **22**, 3378 (2012)
- D.W. Reagor, S.Y. Lee, Y. Li, Q.X. Jia, *J. Appl. Phys.* **95**, 7971 (2004)
- S. Mildner, M. Beleggia, D. Mierwaldt, T. W. Hansen, J. B. Wagner, S. Yazdi, T. Kasama, J. Ciston, Y. Zhu, C. Jooss *J. Phys. Chem. C* **119**, 5301 (2015).
- M.P. Seah, W.A. Dench, *Surf. Interface Anal.* **1**, 2 (1979)
- H.W. Streitwolf, *Ann. Phys. (Leipzig)* **458**, 183 (1959)
- L. Trotochaud, S.W. Boettcher, *Scr. Mater.* **74**, 25 (2014)
- D.G. Truhlar, B.C. Garrett, S.J. Klippenstein, *J. Phys. Chem.* **100**, 12771 (1996)
- M. Varela, M.P. Oxley, W. Luo, J. Tao, M. Watanabe, A.R. Lupini, S.T. Pantelides, S.J. Pennycook, *Phys. Rev. B* **79**, 085117 (2009)
- C.-M. Wang, A. Genc, H. Cheng, L. Pullan, D.R. Baer, S.M. Bruemmer, *Sci. Rep.* **4**, 3683 (2014)
- H. Zandbergen, *Microsc. Microanal.* **18**, 1114 (2012)
- F. Zheng, S. Alayoglu, J. Guo, V. Pushkarev, Y. Li, P.-A. Glans, J.-L. Chen, G. Somorjai, *Nano Lett.* **11**, 847 (2011)
- L. Zhong, X.H. Liu, G.F. Wang, S.X. Mao, J.Y. Huang, *PRL* **106**, 248302 (2011)
- L. Zhong, R.R. Mitchell, Y. Liu, M. Gallant, C.V. Thompson, J.Y. Huang, S.X. Mao, Y. Shao-Horn, *Nano Lett.* **13**, 2209 (2013)
- G. Zhou, L. Luo, L. Li, J. Ciston, E.A. Stach, W.A. Saidi, J.C. Yang, *Chem. Commun.* **49**, 10862 (2013)